Soil & Tillage Research 255 (2026) 106810

Contents lists available at ScienceDirect

Soil & Tillage Research

journal homepage: www.elsevier.com/locate/still

Regulation of soil physical environment and erosion characteristics of farmland by amendments in the black soil region of Northeast China

Xu Leng [a,b,c,d,1], Heng Li [a,b,c,d,1], Qiang Fu [a,b,c,d,*], Tianxiao Li [a,b,c,d,*], Renjie Hou [a,b,c,d], Mo Li [a,b,c,d], Dong Liu [a,b,c,d], Zhaoqiang Zhou [a,b,c,d], Di Wu [a,b,c,d]

[a] *School of Water Conservancy and Civil Engineering, Northeast Agricultural University, Harbin, Heilongjiang 150030, China*
[b] *Joint Laboratory for International Cooperation on Cold Region Black Soil Habitat Health of Ministry of Education, Harbin, Heilongjiang 150030, China*
[c] *Key Laboratory of Effective Utilization of Agricultural Water Resources of Ministry of Agriculture, Northeast Agricultural University, Harbin, Heilongjiang 150030, China*
[d] *Heilongjiang Provincial Key Laboratory of Water Resources and Water Conservancy Engineering in Cold Region, Northeast Agricultural University, Harbin, Heilongjiang 150030, China*

ARTICLE INFO

Keywords:
Amendment
Compound erosion
Hydrothermal environment
Soil structure
Resistance to erosion

ABSTRACT

The unique climatic conditions of the Northeast China's black soil region drive the annual alternation of multiple erosive forces, which damage soil structure. Humic acid (H), lignosulfonate (L), and polyacrylamide (P) are commonly used amendments. However, the mechanism by which amendments regulate erosion under the additive action of freeze-thaw, wind, and rain remains unclear. This study aimed to elucidate how H, L, and P regulate soil hydrothermal dynamics, structural stability, and erosion under compound erosion. Using a self-designed wind tunnel-rainfall simulator, we tested the effects of amendments on aggregate distribution, soil temperature (ST), liquid volumetric water content (LVWC), and sediment yield. The results showed that, compared with control (CK), H, L and P significantly increased the proportion of large and medium-sized aggregates and improved structural stability, thereby enhancing the upper limit of LVWC and ST. When the concentration of L and P increased to 2.0 %, the soil structure became more solid, and the ST fluctuation range decreased by 5.7 %–8.7 %. The cumulative sediment yields of the L and P were reduced by 30.3 % and 99.2 %, respectively, compared with CK. However, the application of H degraded soil physical environment and reduced soil stability as the dosage increased. Compared with the CK, the cumulative sediment yield increased by 28.5 %. Using principal component analysis, we compared the comprehensive improvement effects of different amendments and application rates, and determined that the 2.0 % concentration of P was optimal. These findings provide scientific support for erosion control in Northeast China's black soil areas.

1. Introduction

Soil erosion, driven by water flow, gravity, wind, and freeze-thaw cycles, poses a significant threat to global soil health, water resources, and agricultural sustainability (Lal, 2019). This degradation process is characterized by soil detachment, transport, and deposition, and is exacerbated by the interactions between soil texture, extreme climate conditions (wind blowing, precipitation, freezing, and thawing), topography (slope gradient, slope direction, and slope length), and surface cover (vegetation cover and land cover types) (Li et al., 2019; Zhang et al., 2021). It is estimated that approximately 33.0 % of the world's soils are degraded, with 84.0 % of the land surface affected by erosion (Zhu et al., 2022). In 2021, approximately 2674,200 km^2 of land in China (27.9 % of the total land area) were affected by soil erosion, with some regions experiencing concurrent freeze-thaw erosion, wind erosion, and water erosion, leading to overlapping erosion processes and impacts (Van Pelt et al., 2017; Zhang et al., 2020). For example, the black soil region in Northeast China, characterized by flat terrain, fertile

* Corresponding authors at: School of Water Conservancy and Civil Engineering, Northeast Agricultural University, Harbin, Heilongjiang 150030, China.
E-mail addresses: fuqiang0629@126.com (Q. Fu), litianxiao@neau.edu.cn (T. Li).
[1] Xu Leng and Heng Li contributed equally to the work and should be regarded as co-first authors.

https://doi.org/10.1016/j.still.2025.106810
Received 26 September 2024; Received in revised form 29 July 2025; Accepted 10 August 2025
Available online 18 August 2025

soil, and abundant concentrated precipitation, provides favorable natural conditions for crop growth and is known as China's granary (Wang et al., 2023). However, the region's long and cold winters, with frequent freeze-thaw cycles, alter the bonding between soil particles, disrupt soil structure, and modify its physical properties. These changes affect soil erodibility and infiltration capacity, providing substantial material for other erosive factors and acting as a catalyst for erosion (Starkloff et al., 2017; Wang et al., 2020). Therefore, the interplay of freeze-thaw cycles, rainfall, and strong winds exacerbates the degree of erosion in the region (Sun et al., 2022), directly and indirectly impacting environmental and food security issues. This has already caused significant ecological and economic damage (Borrelli et al., 2023; Marzen et al., 2015).

To reduce runoff and soil loss, researchers have reported that soil amendments can enhance soil structure and improve biochemical properties, thereby increasing erosion resistance (Fangueiro et al., 2018; Liu et al., 2020). Commonly used amendments include lignosulfonate (L), polyacrylamide (P), and humic acid (H). Among these, L, a byproduct of the paper industry, is a non-corrosive, non-toxic, and environmentally friendly chemical amendment (Vinod et al., 2010). L can adsorb negatively charged clay minerals to form a stable soil structure and is widely used to reinforce soil strength and imprfiove erosion resistance (Chen and Indraratna, 2015; Vakili et al., 2018). Turan et al. (2011) reported that L can reduce evaporation in drought and semi-drought-stressed soils, increase water availability for crops, and improve aggregate stability. Liang et al. (2021) conducted the Hole Erosion Test (HET) and found that adding 1.5 % L to sandy soil increased the critical shear stress growth rate of soil samples by 23.2 %. When the L concentration was increased to 3.0 %, the erosion coefficient of cohesive sandy soil samples decreased by 99.8 % (Koohpeyma et al., 2013).

Similarly, P, a high-molecular-weight anionic amendment, enhances soil structure stability and permeability through Ca^{2+}-mediated cation bridging of soil particles, effectively inhibiting soil erosion (Jiang et al., 2010). He et al. (2007) found in wind tunnel experiments that, under the combined action of PAM and water, soils with higher clay content exhibited greater resistance to wind erosion compared to soils with lower clay content. Additionally, the anti-wind erosion effect improved with increasing P concentration. Wei et al. (2011) found that P is non-toxic to plants, and its application increased LVWC by 5.6 %–11.0 % compared to the control, while yield and water use efficiency increased by 14.1 % and 18.4 %, respectively. Additionally, LVWC tended to increase with higher P application concentrations.

Furthermore, H, a natural amendment derived from soil organic matter (Xu et al., 2015), promotes the formation of macroaggregates, improves nutrient content and antioxidant enzyme activity, and enhances drought resistance and nutrient retention capacity, thereby promoting root growth and yield (Cordeiro et al., 2011; Szczerski et al., 2013). Liu et al. (2006) conducted wind tunnel experiments at varying wind speeds and found that the application of H significantly reduced wind erosion by 43.8 %-61.8 %. However, when the concentration of H exceeded 2.0 %, the stability of soil aggregates and soil erosion resistance decreased (Gumus and Seker, 2015).

Although significant progress has been made in the research on soil amendments (L, P, H), most existing studies have focused on the effects of these amendments under single erosion forces (e.g., wind erosion or water erosion alone), neglecting the unique freeze-thaw-wind-water compound erosion processes in the black soil region of Northeast China. This oversight has led to significant deviations in evaluating the true efficacy of amendments in complex environments. Secondly, traditional research has predominantly focused on macroscopic agronomic indicators, lacking systematic analysis of the key mechanisms by which amendments regulate soil water and heat transport, microstructural reorganization, and soil erosion evolution under freeze-thaw cycles. Furthermore, current criteria for selecting amendments are based on single-force experimental data, overlooking the potential synergistic destructive effects that may arise in compound erosion scenarios, where "$1 + 1 > 2$" interactions could occur.

This study employed a self-designed wind tunnel-rainfall simulation device to explore the response mechanisms of soil amendments (L, P, H) to the physical environment, hydrothermal conditions, and erosion characteristics in the black soil region of Northeast China under the superposition of multiple erosion factors. The objectives of this research are: (1) to analyze the regulatory effects of different soil amendments on soil hydrothermal conditions under freeze-thaw cycles; (2) to elucidate the changes and improvements in soil aggregate structure distribution and stability under the superposition of multiple erosion factors; (3) to reveal the evolution patterns of soil runoff and sediment yield under the influence of multiple erosion factors and evaluate the regulatory effects of amendments. The results will provide a scientific basis for further deepening our understanding of the mechanisms by which soil amendments regulate soil erosion and offer theoretical support for optimizing soil conservation and management strategies in the black soil region, with significant ecological and practical application value.

2. Materials and methods

2.1. Overview of the study area

Acheng District is located in the core zone of the typical black soil region in Northeast China, situated at the transition between the western slope of the Zhangguangcai Range uplift and the Songhua River Plain. The region experiences a temperate continental monsoon climate with distinct seasonal variations. Springs are characterized by rapid warming and frequent strong winds, often leading to drought conditions. Summers are short and hot, with abundant rainfall, while autumns see rapid temperature drops and early frosts. Winters are long and cold. The highest recorded temperature in the region is 36.5°C, and the lowest is −38.6°C. Annual rainfall ranges between 500 and 600 mm, with a maximum daily rainfall of 131.1 mm. Rainfall is concentrated from June to September, accounting for approximately 80.0 % of the annual total. The topography is dominated by low mountains, hills, and alluvial plains, with gently sloping ridges and valleys formed by the cutting of Songhua River tributaries. The soil is primarily black soil and chernozem, which is loose and fertile, supporting extensive coverage of temperate meadow steppe, artificial forests, and farmland. The test soil was a 20 cm topsoil layer of arable black soil. The physical and chemical properties, along with the properties of the amendments, are detailed in Table 1.

2.2. Test design

The freeze-thaw simulation test was conducted in an artificial climate chamber developed by the research team with an indoor

Table 1
Material properties of test samples.

Parameters	Soil	Polyacrylamide	lignosulfonate	Humic acid
Sand mass fraction (%)	42.64			
Silt mass fraction (%)	44.75			
Clay mass fraction (%)	12.61			
Organic matter content ($g \cdot kg^{-1}$)	30.15			
pH	6.1			
Cation exchange capacity ($cmol \cdot kg^{-1}$)	2.5			
Bulk density ($g \cdot cm^{-3}$)	1.2			
Field capacity (%)	33			
Molecular weight		12 million		
Property		White powder	Amber powder	Black powder
Water repellent		Soluble	Soluble	Slightly soluble

temperature control range of −20°C to 40°C. The chamber has an embedded control device that automatically adjusts and regulates the indoor environmental conditions over time. The wind-rain simulation test was carried out in the comprehensive test area of the College of Water Conservancy and Civil Engineering at Northeast Agricultural University (Fig. 1).

To create an artificial wind-rain test environment, a wind tunnel-rainfall simulation device was designed (Fig. 1). The wind tunnel-rainfall simulation device measured 2.6 m in length and 0.8 m in width. The wind tunnel simulation module consists of two axial fans, each with a diameter of 0.67 m, an airflow rate of 18,700 $m^3 \cdot h^{-1}$, a maximum rotational speed of 1450 $r \cdot min^{-1}$, a maximum power of 2.2 kW, and a voltage of 380 V. The air velocity was controlled by adjusting the power of each axial fan. The air outlet of each axial fan was connected to a honeycomb channel with a length of 0.4 m and an aperture of 0.1 m. Airflow reached a steady state after passing through the honeycomb channels. The artificial rainfall module consists of an intelligent booster pump and multiple aperture nozzles. The pump has a maximum power of 0.37 kW, a lift of 35 m, and a flow rate of 3.0 $m^3 \cdot h^{-1}$. The nozzle diameters were 1 mm, 1.5 mm, 2 mm, 2.4 mm, and 3 mm, with a spray angle of 40°, and were used to simulate different rainfall intensities ranging from 30 to 240 $mm \cdot h^{-1}$. Mhaske et al. (2019) investigated the relationship between the size and kinetic energy of raindrops upon landing and the corresponding nozzle height. They found that when the nozzle was positioned 2.4 m above the soil surface, the kinetic energy of the raindrops upon landing was similar to the impact force and kinetic energy of natural rainfall. Therefore, the experimental setup in this study adopted this design principle for nozzle installation. The bottom of the simulator is equipped with a slightly sloped catch pan with an outlet pipe to drain excess water that accumulates at the bottom without touching the soil surface. The wind speed uniformity in the wind tunnel-rainfall test device was good, with $\sigma \leq \pm 0.2$ % (σ is the root mean square of the relative deviation of the airflow velocity at any point in the test section), and the wind speed and rainfall uniformity were both greater than 80.0 %.

In this study, a soil trough with a hydraulic jack was also designed to analyze the effects of rainfall on surface runoff and soil erosion. One end of the soil trough is lifted to achieve the desired slope angle by adjusting the hydraulic jack fixed at the bottom of the trough. To simplify the control of variables and avoid the influence of flow continuity and velocity on the precise measurement of soil detachment, a soil flume with dimensions of 400 mm (length) × 400 mm (width) × 200 mm (height) was used in this study. This compact design ensures uniform flow distribution and minimizes edge effects, enabling accurate quantification of soil detachment rates under controlled experimental conditions. Additionally, 8 mm diameter holes were provided at 50 mm intervals along the bottom of the trough for moisture infiltration. When the soil channel is placed in the storm simulator, its outer edge is flush with the lower end of the wind tunnel blades to improve the accuracy and reasonableness of the wind erosion simulation.

2.3. Test program

Considering the local economic benefits and previous research findings, we established two application gradients for the soil amendments (P, L, and H) at 1.0 % and 2.0 %, labeled as P1, P2, L1, L2, H1, and H2, respectively. Treatments without additives were used as the control (CK). Each treatment was replicated three times, resulting in 21 tests (Table 2). In addition, the operation conditions and layout parameters of soil bin filling, maintenance, and erosion simulation are consistent for all treatments. Through long-term field monitoring and simulation, it was observed that the number of daily freeze-thaw cycles (thawing

Fig. 1. Experimental site and installations diagram. (a) represents the experimental site, (b) denotes the wind tunnel-rainfall simulator, and (c) indicates the soil flume and artificial climate chamber.

Table 2
Experimental design for the effect of modifiers on the physical environment and erosion characteristics of soils under the superposition of multiple camping forces.

Treatments	Concentration (%)	Freeze-thaw				Wind tunnel		Rainfall		Slope
		Temperature (℃)		Time (h)	Period	Speed ($m\cdot s^{-1}$)	Time (min)	Intensity ($mm\cdot h^{-1}$)	Time (min)	(°)
		Freezing	Thawing							
P1	1	−20	15	12	13	10	30	100	30	10
P2	2									
L1	1									
L2	2									
H1	1									
H2	2									

during the day and freezing at night) in the 0–20 cm soil layer ranged from 7–12 during the spring thaw period (Wang et al., 2019). Moreover, it was noted that the higher the initial soil water content, the greater the freeze-thaw erosive force (Ferrick and Gatto, 2005). Jiang et al. (2019) also highlighted that slope exceeding 10° in the black soil zone led to the frequent occurrence of fine gully erosion. Therefore, in this test, after removing stones, roots, and other debris from the soil samples, the soil samples were prepared and filled into the troughs based on the soil properties of the 0–20 cm soil layer of the black soil to replicate a natural bare slope with a 10° incline. The LVWC was controlled at 33.0 % and then subjected to 13 freeze-thaw cycles. The freezing temperature for each freeze-thaw cycle was set at −20°C (12 h), and the thawing temperature was set at 15°C (12 h) based on measured ground temperature data and artificial simulations of specific conditions.

Before filling the soil, the bottom of the soil trough was layered with gauze, followed by a 50 mm layer of river sand and another layer of gauze to ensure adequate bottom permeability. The test soil was then uniformly filled in layers at 50 mm intervals using the plate compaction method. Soil interlayer slippage and boundary effects were prevented by roughening each soil layer and compacting the soil around the trench (An et al., 2022). All samples were kept at room temperature for 28 days to allow the soil to condition. To simulate the unidirectional freezing process from top to bottom in a real environment and ensure that changes in the soil structure were similar to those in a realistic setting, the sides and bottoms of the soil troughs were wrapped with 50 mm thick insulation material (Zuo et al., 2022). This insulation material demonstrated good thermal performance (thermal conductivity of 0.017 $W\cdot m^{-1}$) and was removed before the wind-rain simulation test began. When the LVWC of the surface layer (0–10 cm) of the test soil trough decreased to the critical LVWC for wind erosion in black soil (7.0 %) (Liu et al., 2017), the trough was placed in the wind tunnel-rainfall simulator to conduct the erosion test, starting with wind erosion followed by rainfall erosion. The test rainfall intensity and wind speed were determined by observing high-intensity, short-duration, erosive rainstorms and wind events in the test area, as shown in Table 2.

2.4. Measurement of indicators

2.4.1. Soil hydrothermal

A soil moisture, temperature, and salinity sensor (HydraProbe II, Stevens Co., Ltd., America) was installed at 50 mm depth within the soil trough to record data every 30 s, monitoring changes in soil moisture content and temperature.

2.4.2. Soil water stability aggregates

To study the effects of soil amendments on soil aggregates during composite erosion, 50 g of soil sample was wet-sieved and classified using a water-stable aggregate analyzer to obtain four types of aggregates: large aggregates (> 2 mm), medium aggregates (0.25–2 mm), small aggregates (0.106–0.25 mm), and silt and clay (< 0.106 mm). The soil aggregate stability was evaluated using the mean weight diameter (MWD, mm), fractal dimension (D), and failure index (K) (Xue et al., 2022). The larger the MWD value is, the more stable the soil structure and the less likely the loss of soil nutrients; the smaller the D value is, the better and more stable the soil aggregate structure; and the smaller the K value indicates better soil erosion resistance and higher soil fertility. The calculation formula is as follows:

$$MWD = \sum_{i=1}^{n} \overline{x_i} W_i \tag{1}$$

$$\frac{M(r < \overline{x_i})}{M_T} = \left[\frac{\overline{x_i}}{x_{max}}\right]^{3-D} \tag{2}$$

$$K = 7.954 \times \left\{ 0.0017 + 0.0494 \times \exp\left[-0.5 \times \left(\frac{1.675 + \lg\left(\exp \sum_{i=1}^{n} \ln \overline{x_i}\right)}{0.6986} \right)^2 \right] \right\} \tag{3}$$

where x_i is the average diameter with respect to size, mm; W_i is the percentage of the total volume of the corresponding granular aggregate x_i,%; M_T is the total weight of the agglomerates, g; $M(r < x_i)$ is the percentage of the mass of the aggregates smaller than x_i,%; and x_{max} is the maximum particle size of the aggregate, mm.

In addition, a field emission scanning electron microscope (FE-SEM SU81010, Hitachi Co., Ltd., Japan) was used to determine the microscopic characteristics of the soil samples.

2.4.3. Soil moisture characterization curves and parameters

Soil water characteristic curves (SWRCs) were developed to analyze soil water retention. Each in situ soil sample was immersed in a water storage container for 12 h to reach saturation. Different SWRC treatments were performed using a high-speed refrigerated centrifuge (CR21GIII, Japan) at room temperature (25°C). A total of 12 substrate suction units were set (0, −0.01, −0.03, −0.05, −0.1, −0.33, −0.5, −1, −3, −5, −10, and −15 bar). After the set equilibrium time was reached, the soil was weighed using an electronic balance and dried in an oven at 110°C for 12 h. The volumetric water content corresponding to each suction value was determined. The relationship between matric potential and volumetric water content, as obtained by fitting the van Genuchten model, represents the SWRC. Additionally, the soil moisture characteristic parameters were calculated based on the soil moisture characteristic curve, which includes three indicators: field capacity (FC, defined as the volumetric soil water content after equilibrium when the matric potential is −0.33 bar $\theta(h)$, $cm^3\cdot cm^{-3}$), permanent wilting point (PWP, soil volumetric water content $\theta(h)$, $cm^3\cdot cm^{-3}$ when the matric potential is −15 bar), and plant available water content (PAWC, calculated as the difference between the FC and PWP). The V-G model is expressed as follows:

$$\theta(h) = f(x) = \begin{cases} \theta_r + \dfrac{\theta_s - \theta_r}{[1 + |\alpha \cdot h|^n]^m}, h < 0 \\ \theta_s, h > 0 \end{cases} \tag{4}$$

where h is the negative pressure of the soil in H_2O; $\theta(h)$ is the volumetric water content of the soil under the corresponding pressure, %; θ_r is the residual volumetric water content, %; θ_s is the saturated volumetric water content, %; α is the reciprocal of the intake value, cm^{-1}; n and m are parameters characterizing the shape of the curve, m = 1–1/n, and the above parameters were obtained by fitting with the RETC software.

2.4.4. *Determination of erosion characteristics indicators*

The weight difference of soil samples in wind tunnel experiments is defined as wind erosion mass. Wind action transported exposed soil particles from the CK and H into the extensive cracks formed by freeze-thaw cycles, thereby reducing measurable wind erosion. In contrast, the L and P treatments maintained stable soil structures, resulting in minimal differences in wind erosion rates among all treatments. However, the accumulated particles within cracks served as a substantial sediment source for rainfall-induced erosion. To investigate compound soil erosion processes, this study focused primarily on sediment yield dynamics under the interactive effects of wind detachment and rainfall impact. Following the rainfall, the supernatants are separated, and the sediment is dried in a 105°C oven to measure sediment quality. The runoff, sediment yield, cumulative runoff, and cumulative sediment yield are calculated for each period. Post-erosion surface roughness assessment was conducted using the chain method (Thomsen et al., 2015) across five randomly selected locations within the soil flume. At each location, the calibrated chain was carefully positioned to conform to the soil microtopography, and horizontal span measurements were recorded at five predetermined points. The surface roughness was calculated using the standardized chain method equation:

$$C_r = [1 - L_2/L_1] \times 100\% \tag{5}$$

where C_r is the surface roughness; L_1 is the original chain length (mm); L_2 is the horizontal length of the chain after it is placed on the slope and shortened (mm).

2.5. *Statistical analysis*

The test data were organized using Microsoft Excel 2016 and analyzed with SPSS 26 software. One-way analysis of variance (ANOVA) was employed to compare differences between treatments. A significance level of $p < 0.05$ was considered statistically significant for all analyses. Data visualizations were generated using Adobe Illustrator 2022 and Origin 2021.

3. Results

3.1. *Changes in soil hydrothermal environment in different treatments*

3.1.1. *Soil temperature*

Freezing and thawing alternations directly affect ST, resulting in an extreme cyclic change in ST resembling an "Λ" shape. The range of ST fluctuations in the CK exhibited an upward-decreasing cycle dynamic shift with an increasing number of freeze-thaw cycles. the magnitude of the change stabilized at the end of the tenth freeze-thaw cycle (Fig. 2c). Compared with the CK, the amendments significantly increased the ST. The addition of humic acid (H), lignosulfonate (L), and polyacrylamide (P) raised the ST lower limit by an average of 7.2 %, 15.9 %, and 14.7 %, respectively, and the ST upper limit by 21.8 %, 27.5 %, and 55.4 %, respectively. As shown in Fig. 2a and b, there was a two-level change in the insulation effect of different amendments with increasing concentration, with H2 reducing the ST upper limit by an average of 3.2 % and increasing the ST lower limit by 3.2 % compared with H1. The insulation effects of L2 and P2 remained relatively stable, and the differences from those of L1 and P1 gradually increased after multiple freeze-thaw cycles. The ST upper limits decreased by an average of 0.8 % and 2.6 %, respectively, while the ST lower limits increased by 14.2 % and 8.3 %, respectively.

As shown in Fig. 2c, L1 effectively reduced the fluctuation amplitude of the ST and narrowed its variation range. P1 and H1 demonstrate excellent thermal conductivity but poor insulation properties, leading to an increase in the range of ST fluctuations. In comparison to P1, H1, and CK, L1 decreased the ST range by 9.4 %, 3.9 %, and 2.0 %, respectively. Moreover, the ST range showed a negative correlation with the

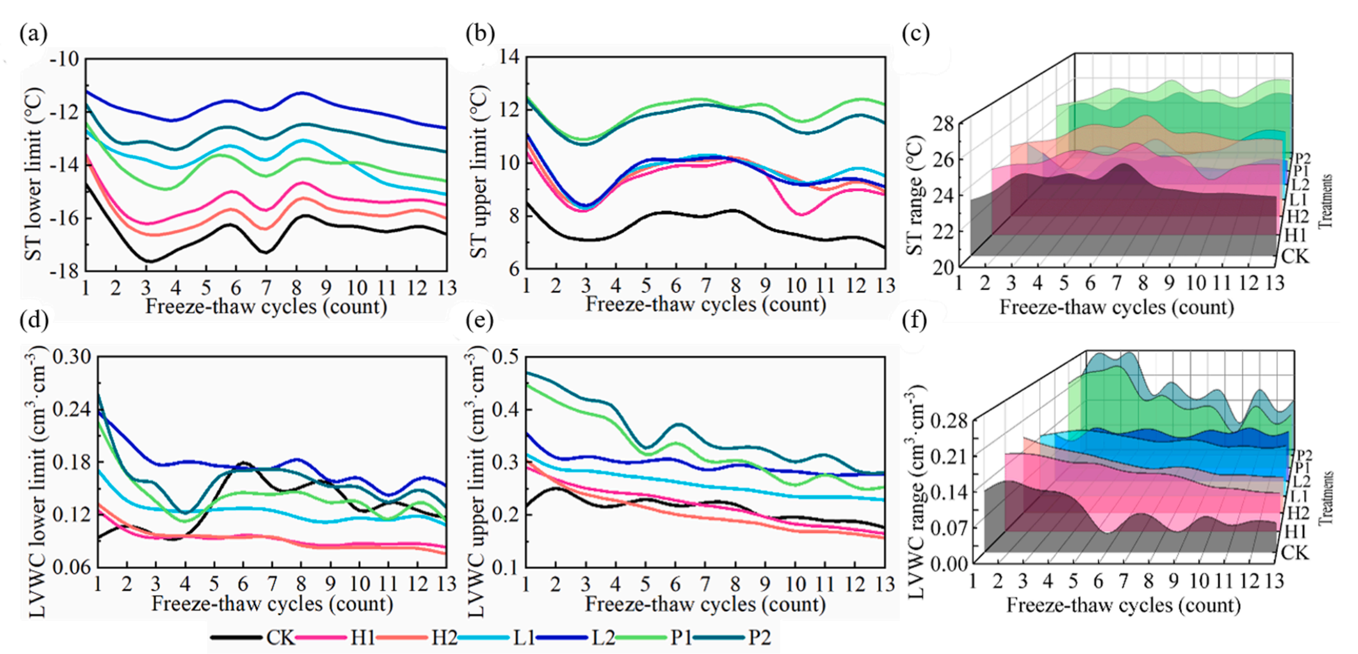

Fig. 2. Changes in the soil hydrothermal environment during the freeze-thaw cycle. (a) and (d) represent the lower limit of soil temperature (ST) and liquid volumetric water content (LVWC) during each freezing phase (12 h), whereas (b) and (e) denote the upper limit of ST and LVWC during each thawing phase (12 h). (c) and (f) indicate the fluctuation range of ST and LVWC over each freeze-thaw cycle (24 h).

concentrations of L and P. The ST ranges of L2 and P2 were 8.7 % and 5.7 % lower than those of L1 and P1, respectively. While the ST range continued to rise with an increase in H concentration, H2 increased by an average of 3.2 % over H1.

3.1.2. Soil volumetric water content

The LVWC and ST exhibit similar trends. During the freezing period, water condenses into ice, leading to a decrease in LVWC. Conversely, during the thawing period, the water transitions back to liquid state, resulting in an increase in LVWC. With an increase in the number of freeze-thaw cycles, the soil structure undergoes changes, and the range of water content fluctuations varies. As shown in Fig. 2d and e, the upper and lower limits of the LVWC of CK reached their peak values during the second and sixth freeze-thaw cycles, respectively, before gradually declining. The addition of amendments can notably enhance soil water retention, particularly towards the end of the initial freeze-thaw cycle, with the upper limit of LVWC increasing by an average of 61.4 % compared to CK. However, as the number of freeze-thaw cycles increases, the water retention capacity of each amendment diminishes. By the conclusion of the freeze-thaw test, the upper limit of the LVWC for H1 decreased by 43.2 %, and comparison to CK, the upper and lower limits of the LVWC decreased by 6.2 % and 28.9 %, respectively, indicating a subpar water retention effect. The LVWC fluctuation range for L1 remained relatively stable, decreasing by only 6.5 % at the end of the freeze-thaw test (Fig. 2f). The upper limit of the LVWC for L1 decreased by 24.5 %, which was 29.6 % higher than that of CK, demonstrating favorable water retention performance. The upper limit of the LVWC for P1 consistently exceeded that of the other treatments, with the widest fluctuation range, decreasing significantly with increasing freezing and thawing cycles. By the end of the freeze-thaw test, the upper limit of the LVWC for P1 decreased by an average of 43.4 %, and the LVWC range narrowed by 50.0 %. Nevertheless, the upper limits of the LVWC for P1 remained 10.8 %, 53.1 %, and 43.6 % higher than those of L1, H1, and CK, respectively, showcasing superior water retention performance.

With increasing concentration, the upper limits of the LVWC of P2 and L2 increased by 9.2 % and 14.4 %, respectively, while the lower limits of the LVWC increased by 13.2 % and 40.9 %, respectively, compared to those of P1 and L1. The maximum LVWC value for this test was recorded at P2 (47.1 %), significantly exceeding the 33.0 % specified for the test requirements. In comparison to H1, the upper limit of the LVWC for H2 decreased after the second freeze-thaw cycle, with an average decrease of 7.0 %. Following the sixth freeze-thaw cycle, the lower limit of the LVWC dropped below that of H1, with an average decrease of 4.2 %. Additionally, based on Fig. 2d, the difference in the upper limit of the LVWC between P2 and L2 decreased as the number of freeze-thaw cycles increased, with a 0.9 % increase by the end of the test. Conversely, the lower limit of the LVWC for P2 started to fall below that of L2 after the first freeze-thaw cycle, with an average reduction of 10.8 %. L2 exhibited an average LVWC floating range that was 35.6 % smaller than that of P2. Although L2 did not retain as much water as P2, it demonstrated better stability.

3.2. Changes in soil structure in different treatments

3.2.1. Characteristics of the soil bulk density and aggregate distribution

The soil was gradually compacted under the action of compound erosion, resulting in an increase in the soil bulk density (BD). The BD was 15.7 % greater in the CK than in the initial test design. Soil amendments can improve soil structure and properties, decrease the soil BD, increase the soil porosity, and enhance the soil stability. Compared with the BD of the CK, those of H1, P1 and L1 were reduced by an average of 4.3 %, 7.6 % and 10.2 %, respectively. As shown in Fig. 3b, the BD of H and L tended to decrease with increasing improver concentration, with average increases of 3.2 % and 5.0 % in the BD of H2 and L2, respectively, compared with those of H1 and P1 ($p < 0.005$). The BD of P tended to increase, and the BD of P2 was 5.0 % lower than that of P1 ($p < 0.005$).

The unique cementation and adsorption properties of soil amendments transform microaggregates into large aggregates, significantly increasing the particle size of soil aggregates. As shown in Fig. 3a, the percentage of > 0.25 mm agglomerates in H1, P1, and L1 increased by 124.9 %, 259.4 %, and 357.9 %, respectively, compared with that in the CK on average ($p < 0.005$). Additionally, the percentage of < 0.25 mm agglomerates decreased by 25.1 %, 52.1 %, and 71.9 %, respectively, compared with that in the CK on average ($p < 0.005$). As the concentration of the same amendment increased, the impact on the soil aggregates varied significantly. The proportion of agglomerates above 2 mm in P2 and L2 increased by 15.7 % and 28.4 %, respectively, on average in P1 and L1, while the proportion of agglomerates below 2 mm decreased by 51.3 % and 42.8 %, respectively, on average ($p < 0.005$).

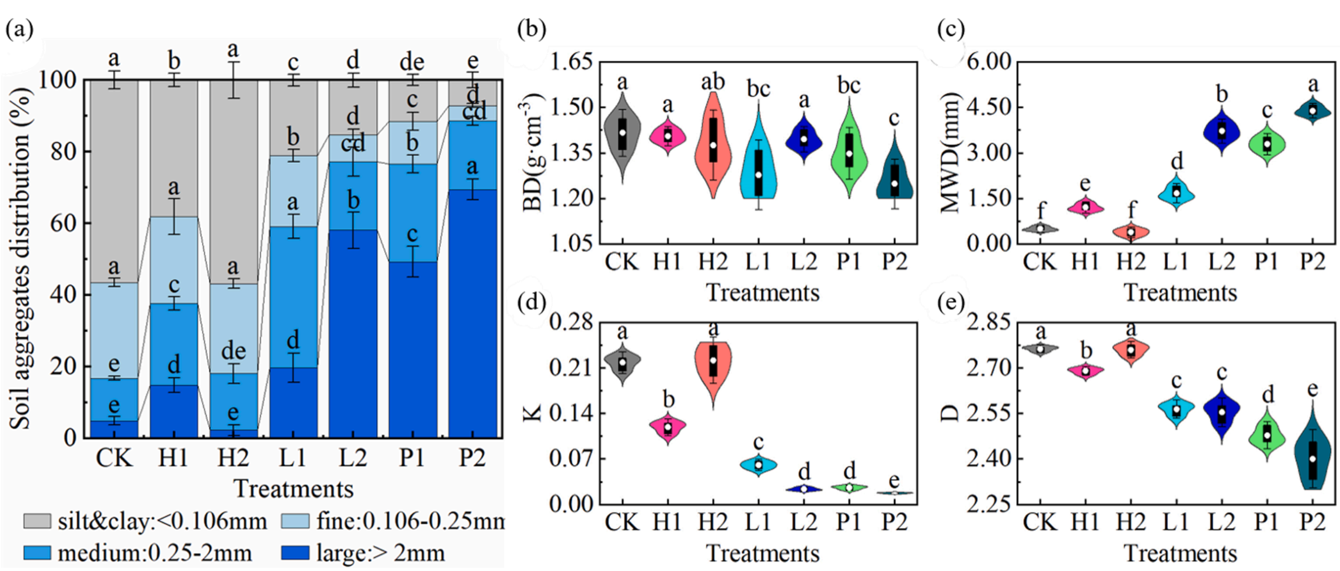

Fig. 3. Soil water-stable aggregate size distribution and stability index. (a) and (d) represent the cluster distribution and soil bulk density (BD), respectively, (c) and (e) indicate the mean weight diameter (MWD), failure index (K), and fractal dimension (D), respectively. Different lowercase letters in the same line in (a) and versus different lowercase letters in (b)-(e) all indicate significant ($p < 0.05$) differences in the same grain size across treatments, and parameters labeled with the same letter are not significantly different.

Conversely, for H, the percentage of > 0.25 mm agglomerates decreased by 52.1 %, and the percentage of < 0.25 mm agglomerates increased by 31.4 % with increasing concentration ($p < 0.005$). In conclusion, the application of soil amendments can enhance the formation of large aggregates, and the efficiency of reconstructing aggregates improves with increasing concentration. However, surpassing a certain threshold in the application of specific amendments (such as H) leads to a significant decrease in the enhancement effect.

3.2.2. Soil aggregate stability

The aggregate stability indices of different ameliorator-treated soils under the superposition of multiple compaction forces were calculated based on the distribution of water-stable aggregates (Fig. 3b–d). In this case, the soil mean weight diameter (MWD) was utilized to describe the size of the soil aggregates. The application of the soil amendments significantly improved the MWD. However, due to the varying mechanisms and effectiveness of different amendments in improving soil structure, there were differences in the proportions of large aggregates in the soil, leading to varying effects on aggregate stability. Compared to the CK, the MWD in H1, L1, and P1 increased by 140.2 %, 233.1 %, and 554.0 %, respectively ($p < 0.005$). The failure index (K) indicates the extent of damage to soil aggregates under erosion. The K values of H1, L1, and P1 were 45.5 %, 72.1 %, and 88.0 % lower ($p < 0.005$) than that of CK, respectively, showing a significant increase in erosion resistance. The fractal dimension, D, reflects the uniformity of soil aggregates and is a more sensitive and accurate parameter for evaluating aggregate characteristics. The different amendments decreased the D value and enhanced soil stability. Compared with CK, D was reduced by 2.6 %, 7.2 %, and 10.3 % for H1, L1, and P1, respectively ($p < 0.005$).

The MWD of P and L increased with rising concentration, showing a 33.4 % and 121.9 % increase for P2 and L2, respectively, compared to P1 and L1 ($p < 0.005$). Conversely, both K and D exhibited a decreasing pattern, with K decreasing by 31.8 % and 60.6 % ($p < 0.005$), and D decreasing by 3.1 % ($p < 0.005$) and 0.4 % ($p > 0.005$) for P2 and L2, respectively. As the concentration of H increased, the number of large aggregates in the soil decreased, while the number of small and medium aggregates increased, leading to reduced soil stability. In comparison to H1, the MWD of H2 decreased by 67. 9 %, and those of K and D increased by 86.5 % and 2.6 %, respectively ($p < 0.005$). The soil stability of H2 was inferior to that of CK.

3.3. Changes in soil erosion characteristics in different treatments

3.3.1. Runoff

Runoff increased rapidly with longer durations of rainfall for the different treatments (Fig. 4a). The CK peaked at 7.2 kg during the 3–6 min period, after which there were no significant fluctuations in runoff until the end of the rainfall. Soil amendments can help slow down the increasing trend of runoff. The trends of H1 and CK were similar, reaching a peak value in the 9–12 min period and remaining relatively stable thereafter. The maximum runoff of H1 decreased by an average of 1.4 % compared to the CK treatment, but as the H1 concentration increased, the runoff also increased. In comparison to H1 and CK, the maximum runoff of H2 increased by 2.8 % and 1.4 %, respectively. The high water absorption capacity of P could delay the onset of runoff, with runoff showing a rapid increase followed by a gradual leveling off. However, as the concentration increased, the maximum runoff of P2 increased by 47.2 % compared to P1, while the maximum runoff of P2 and P1 decreased by 50.0 % and 26.4 %, respectively, compared to CK. At the beginning of runoff generation (0–9 min), the runoff of L is low and stable. However, after 9 min, runoff increases rapidly, with L1 showing a much greater increase than L2. There is a 43.4 % increase in maximum runoff and a 5.1 % increase in runoff during the 27–30 min period compared to P2.

The amendments could cause a lag in peak runoff and reduce total runoff. L decreased the runoff with increasing concentration, and L2 had the lowest total runoff of 11.95 kg, which was 54.0 % and 82.0 % lower than those of L1 and CK, respectively. P had the same flow stopping effect, but its ability decreased with increasing concentration. The total runoff of P2 increased by 80.4 % compared with that of P1 but decreased by 34.9 % compared with that of CK. As shown in Fig. 4c, the total runoff of H1 decreased by 2.9 % compared with that of CK. However, with increasing H2 concentration, the total runoff of H2 even increased by 1.8 % compared with that of CK.

3.3.2. Runoff sediment production

The drenching of rainfall and the washing of runoff carry some of the sediment away from the soil, causing erosion. As shown in Fig. 4b, the sediment yield for CK rapidly increased with increasing rainfall duration, reaching a peak (0.44 kg) within the 3–6 min period and then quickly decreased until it stabilized. As the amendments were applied,

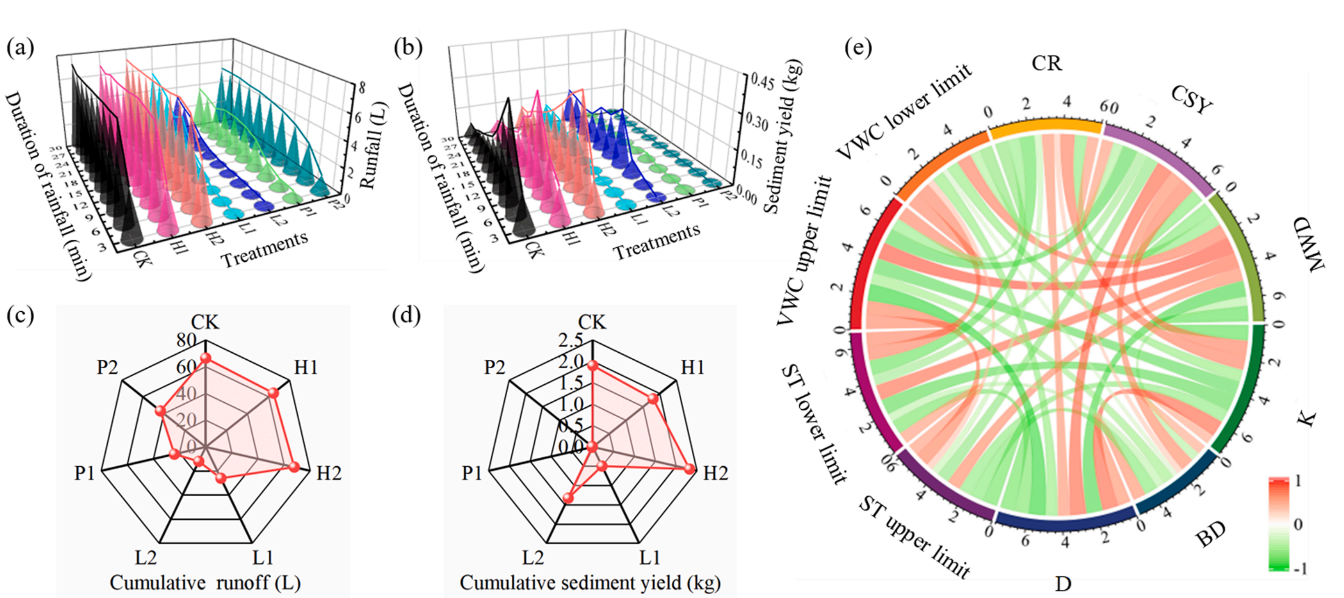

Fig. 4. Soil runoff, sediment yield, and their correlation with soil water, heat, and aggregate stability index. (a) and (b) represent runoff and sediment yield in different periods, (c) and (d) denote cumulative runoff (CR) and cumulative sediment yield (CSY), and (e) indicates the correlation between CR, CSY, and soil water, heat, and stability index.

the soil structure stability increased, and the sediment yield decreased. H1 peaked in terms of sediment yield at 6–9 min intervals and then decreased quickly, by 5.0 %, compared with the peak of the CK. When the concentration increased, the control effect of H2 decreased, the sediment yield trend was closer to that of the CK, and the sediment yield was greater than that of the CK in all periods from 6–30 min. At the end of the rainfall period, the total sediment yield of H2 was 21.9 % and 28.5 % greater than that of H1 and CK, respectively. Compared with H1, L1 significantly suppressed the growth rate of the sediment yield and reduced its upper limit. However, as the L2 concentration increased, the hysteresis effect weakened, and the sediment yield increased. Compared with that of L1, the total sediment yield increased by 1.7 %, but it was 30.3 % lower than that of CK. Compared with L1 and H1, P1 provided the best erosion control, with a slow increase in runoff erosion throughout the rainfall test. The sediment yield was less than 0.05 kg in each period. With increasing concentration, no significant change in sediment yield was observed. Compared with that in P1, the total sediment yield in P2 was 1.9 % lower but 99.2 % lower than that in CK.

Fig. 4e shows the correlation matrix of the 10 indicators. Overall, all indicators were significantly correlated. Total runoff and total sand production being significantly positively correlated with D, BD, and K, and significantly negatively correlated with the other indicators. The results indicated that changes in soil erosion characteristics are closely linked to the stability of soil aggregates. The more stable the soil aggregates' structure, the greater the erosion resistance. The study calculated the contributions of various treatments using principal component analysis (Shao et al., 2023) to evaluate different soil amendments. To simplify the indicators, the 10 indicators were condensed into Y1 and Y2. The proportion of the corresponding eigenvalues of each principal component to the total eigenvalues of the extracted principal components was used as a weight to calculate the comprehensive evaluation model of the principal components: $Y = 0.8671Y1 + 0.1330Y2$. Table 3 shows that P2 has the highest composite ranking, while H2, H1, and CK have negative composite contributions. In terms of enhancing the physical environment of soil with erosion resistance, the combined improvement effect of P was superior to that of L and H.

4. Discussion

4.1. Mechanism by which amendments regulate the soil hydrothermal environment under freeze-thaw cycles

Freeze-thaw cycles significantly alter soil moisture dynamics by modifying pore structure. During freezing, water phase transitions generate ice crystals that create large frozen pores, while thawing leads to ice melt and the formation of interconnected thawed pores. This dynamic evolution of pore structure directly impacts soil aeration and water retention properties (He et al., 2019; Zhao and Hu, 2023). The application of soil amendments improves soil permeability, enhances porosity, and promotes water infiltration and cycling, thereby increasing soil water-holding capacity (Sarker et al., 2022). As shown in Fig. 5c, the saturated volumetric water content (θs) and field capacity (FC) were significantly elevated. This inverse evolution of hydrological parameters is closely linked to the enhanced pore connectivity induced by freeze-thaw cycles. The regulatory mechanisms of different amendments on water retention exhibited marked variability (Fig. 5a). For instance, the low water solubility of H led to molecular self-aggregation at excessive application rates (H2), forming microspheres rather than effectively binding soil particles. These structural defects generated tensile cracks during freeze-thaw cycles, increasing water evaporation flux and resulting in a lower LVWC for H2 than the CK. Specifically, θs, FC, and plant available water content (PAWC) decreased by 3.2 %, 0.9 %, and 22.2 %, respectively, while the permanent wilting point (PWP) increased by 2.0 % (Fig. 5c). These observations align with the synergistic microbial degradation effects reported by Park et al. (2015), collectively explaining the accelerated decline in water retention capacity under H treatment.

In contrast, the hydrolysis of L and P in soil forms a hydrogel film on soil particle surfaces (Li et al., 2023; Rodrigues Sousa et al., 2021). This film enhances water-binding energy through hydrogen bonding and van der Waals forces, significantly improving water retention in the low-suction range—a mechanism consistent with the reduced evaporative losses reported by Xue et al. (2022). Notably, the unique polymer chains of P reduce water surface tension, forming a denser adsorbed water layer (Adjuik et al., 2022), which explains the higher LVWC upper limit for P1 compared to L1 in this study. Additionally, the hydrogel films formed by P and L retain water during freezing and release it upon thawing, effectively mitigating moisture loss and maintaining higher LVWC even after multiple freeze-thaw cycles. Consequently, the LVWC thresholds for P and L treated soils were significantly higher than those for H and CK.

With increasing amendment concentrations, L and P form thicker hydrogel films, enhancing adhesion and water absorption capacity. Notably, the polymer chains of P elongate at higher concentrations, further amplifying its water retention capability (Chen et al., 2016). Compared to L1 and P1, L2 and P2 improved θs and FC by 6.5 % and 35.1 %, and 6.9 % and 41.4 %, respectively. However, excessive film thickness elevated water-binding energy, surpassing the average water absorption potential of plant roots (Ariyanta et al., 2023; Mulualem et al., 2021), resulting in a 67.1 % and 93.2 % increase in PWP and a 38.7 % and 47.9 % reduction in PAWC for L2 and P2, respectively.

A critical finding was that during the first four freeze-thaw cycles, the LVWC of P treated soils exceeded the initial designed moisture content, surpassing other treatments. This phenomenon is attributed to soil water redistribution, where surface moisture diffuses under gravitational forces during thawing. The strong water-absorbing capacity of P, aided by capillary action, adsorbed free water, thereby increasing LVWC (Liu et al., 2022; Wang et al., 2022). As freeze-thaw cycles progressed, water redistribution amplified differences between treatments. Notably, the lower LVWC threshold of P2 compared to L2 was linked to P2's adsorption on soil particles, which slowed water migration and ice crystal growth near the freezing front. Ji et al. (2023) used desiccation methods to evaluate soil moisture distribution and reported that higher P concentrations reduced the maximum water content at the freezing front from 53.4 % to 31.4 %. In contrast, L exhibited higher water redistribution efficiency, more stable water retention, and thermal hysteresis effects (Khajeh et al., 2024; Yang et al., 2024), leading to a gradual convergence in LVWC differences between L and P.

The ST is directly influenced by freeze-thaw cycles and indirectly regulated by factors such as the LVWC (Wu et al., 2023). Previous studies have shown that soils with higher moisture content exhibit slower temperature fluctuations under identical thermal inputs due to their greater heat capacity and thermal conductivity (Lu et al., 2007). This means that in high-temperature environments, regions with higher moisture content warm more slowly, while in low-temperature environments, these regions also cool more gradually (Abu-Hamdeh, 2003; Lu et al., 2014). This attenuation of temperature fluctuations primarily originates from freeze-thaw-mediated pore restructuring. During this process, ice-phase-transition stresses increase soil bulk density and thermal conductivity through structural modifications, thereby

Table 3
Ranking of combined contributions determined by principal component analysis.

Treatments	Y1	Y2	Y	Ranking
CK	−3.2902	0.6147	−2.7711	7
H1	−2.1200	−0.2393	−1.8700	5
H2	−3.0681	−0.7112	−2.7548	6
L1	0.8450	−0.5749	0.6562	4
L2	1.9460	2.1108	1.9680	2
P1	2.0971	−0.0130	1.8166	3
P2	3.5902	−1.1870	2.9551	1

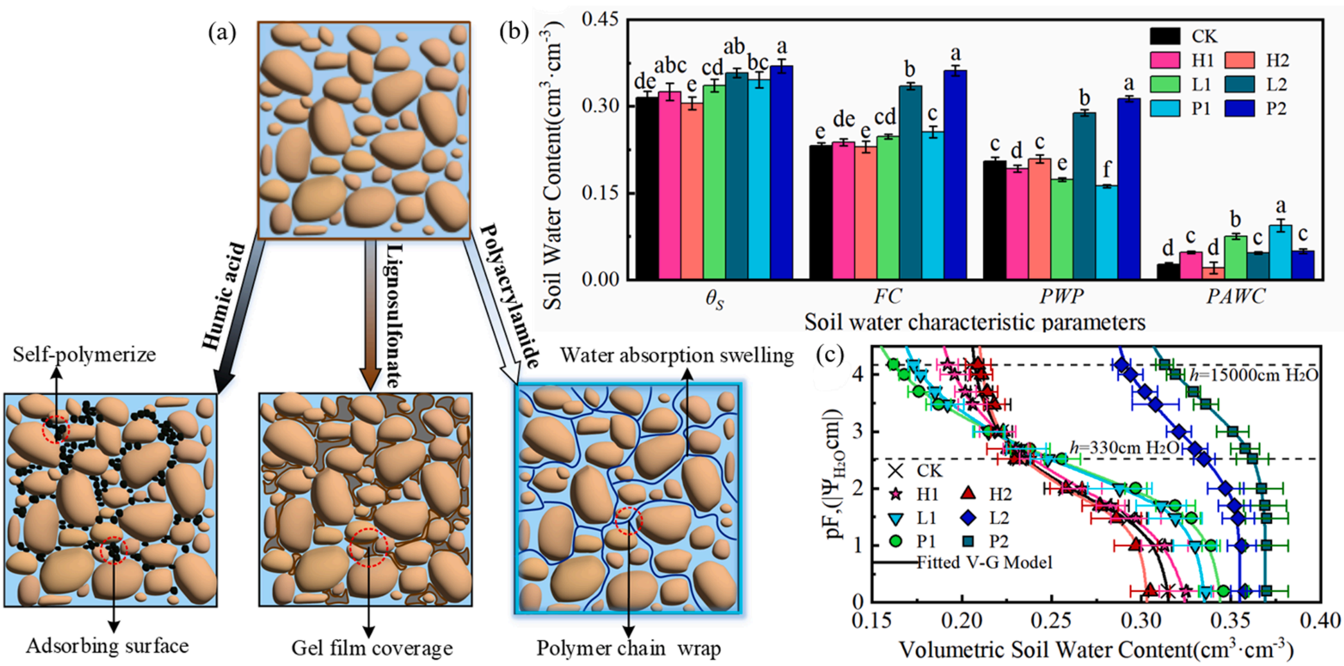

Fig. 5. Schematic diagrams for stabilization mechanism of amendments and soil moisture characteristics. (a) represents the stabilization mechanisms of humic acid, lignosulfonate, and polyacrylamide, while (b) and (c) depict the moisture characteristic curve and its associated parameters, respectively.

enhancing heat capacity and consequently suppressing thermal variability.

Notably, soil amendments significantly alter this process by modulating hydrothermal coupling mechanisms. The inhibitory effects of amendments on temperature fluctuations vary markedly due to their distinct functional mechanisms (Fig. 2a, b). Treatments with P and L reduce interfacial thermal resistance and enhance heat capacity by forming hydrogel films. Additionally, their hydrogen-bond networks convert free water into bound water, minimizing latent heat loss during phase transitions (Jiang et al., 2024). P, with its unique polymer chains, exhibits higher thermal conductivity but lower phase change enthalpy, thereby weakening its low-temperature protective capacity. In contrast, H demonstrates inferior water retention, thermal insulation, and heat capacity.

With increasing concentrations of L and P, the formation of thicker protective hydrogel layers further enhances soil heat capacity and reduces temperature fluctuations. The thickening of these hydrogel films not only amplifies thermal hysteresis but also suppresses heat loss from the soil to the atmosphere, thereby minimizing moisture loss and slowing freezing rates during freeze-thaw cycles. As a result, the upper limit of ST gradually decreases, while the lower limit progressively increases (Andry et al., 2009; Jiang et al., 2024).

However, excessive water absorption and swelling in P2 create numerous pores, which enhance air flow and accelerate heat loss compared to L2, ultimately reducing its thermal insulation efficiency. In contrast, H2 exhibits molecular self-aggregation, leading to crack formation. This reduces soil heat capacity, water retention, thermal insulation, and the ST lower limit, while increasing thermal conductivity and the ST upper limit (Turan et al., 2011). These findings demonstrate that freeze-thaw cycles dynamically regulate soil hydrothermal processes through pore structure reorganization, while the type and concentration of amendments dictate the direction and magnitude of these effects.

4.2. *Regulation effects of amendments on soil structure and erosion under multi-force interactions*

The coupling of freeze-thaw, wind, and water erosion processes significantly compromises soil structural integrity through multiple pathways. Freeze-thaw cycles induce volumetric expansion-contraction of the soil matrix, triggering dynamic reorganization of pore structures and redistribution of soil particles (Liu et al., 2023; Xue et al., 2022). This mechanical disturbance breaks down large and medium aggregates into finer particles, which are subsequently subjected to wind erosion and compaction under raindrop impact, increasing soil BD. The application of soil amendments enhances interparticle friction and forms an integrated matrix, preventing the formation of tensile cracks. Additionally, the cementing and adsorption properties of amendments bind soil particles or micro-aggregates into larger aggregates, promoting a transition from a particle-based structure to a more aggregated one (Tajdini et al., 2018). Our experimental results demonstrate that P, L, and H effectively promote the aggregation of particles > 0.25 mm through distinct stabilization pathways, enhancing aggregate stability and counteracting these degradation mechanisms. H enhances aggregate stability by forming physico-chemical bonds with mineral-organic complexes through active functional groups (-COOH, -OH) (Semenov et al., 2013). However, dose-dependent effects become evident: at low concentrations (H1), H increases soil compactness by 8.7 % through pore filling. When the concentration increases to 2.0 % (H2), compactness decreases by 21.2 % compared to H1, accompanied by reduced aggregate stability. This reversal may arise from two mechanisms: (1) thick organic layers at high doses increase interparticle distances, weakening van der Waals forces; (2) competitive cation complexation by H disrupts ionic bridges between clay particles(Semenov et al., 2013).

In contrast, the L amendment demonstrates superior cementing capabilities through macromolecular bridging effects. Scanning electron microscopy (SEM) observations reveal that its flaky structure, characterized by sharp edges, effectively locks aggregates within the pore network (Ta'negonbadi and Noorzad, 2017). Thus, L enhances soil stability and compactness by hydrolyzing colloids to coat particle surfaces and geometrically matching pore sizes, achieving mechanical interlocking of aggregates. As shown in Fig. 6h, L1 increased soil compactness by 49.6 % compared to the CK, and with increasing concentration, L2 further improved compactness by 27.7 %, consistent with the findings of Dong et al. (2023). Notably, P exhibits the most pronounced structural enhancement. As water evaporates, P's rigidity increases, leading to higher soil compactness. In this study, P1 increased

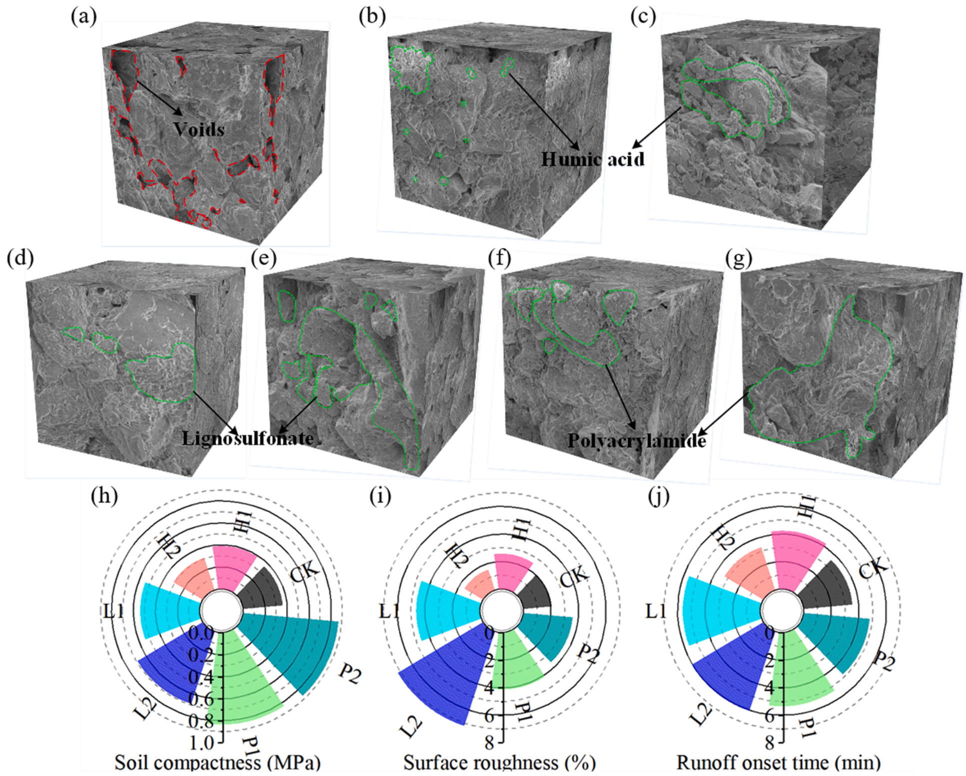

Fig. 6. Soil surface characteristics and runoff onset time. (a)-(g) represent schematic structures of CK, H1, H2, L1, L2, P1, and P2, respectively, and (h)-(j) denote soil compactness, surface roughness, and flow production time, respectively.

compactness by 131.8 % compared to CK. This is primarily attributed to the dual mechanisms of P: (1) physical entanglement of polymer chains reducing surface tension, and (2) chemical bonding via functional groups, forming hydrogel films that encapsulate aggregates (Chen et al., 2016). With increasing concentration, the hydrogel layer thickens, and polymer chains elongate, resulting in a more stable soil structure. This is evidenced in SEM images by a reduction in exposed aggregates (Fig. 6g).

Repeated freeze-thaw cycles reduce structural stability while increasing susceptibility to wind and water erosion (Leuther and Schlueter, 2021; Sun et al., 2022). In this experiment, H and CK soils developed large interconnected cracks on their surfaces. Wind-transported fine particles were deposited into these cracks, significantly reducing wind erosion rates. In contrast, L and P soils exhibited only minor cracks, higher compactness, and fewer exposed particles, effectively suppressing wind erosion. Consequently, no significant differences in wind erosion rates were observed among treatments. Freeze-thaw-induced cracks accelerated lateral rainwater infiltration, causing rapid soil saturation and earlier runoff initiation (Fernandez-Raga et al., 2017; Zhang, 2023). Fine particles within cracks provided abundant erodible material for rainfall scouring, resulting in sediment yields that reflect combined wind and water erosion effects. Under continuous raindrop impact, fine particles in H and CK soils were transported and deposited on the surface, forming a dense crust that impeded infiltration, increased surface runoff, and reduced surface roughness and sediment yield (Kinnell, 2022; Sela et al., 2014). H1 delayed runoff initiation and reduced sediment yield through partial cementation. However, H exhibited concentration-dependent structural degradation, leading to excessive soil loosening. Simultaneously, preferential flow path development induced hydraulic anisotropy, causing H2 to initiate runoff earlier and increase sediment yield.

Compared to H, the elongated cracks in L1 increased the tortuosity of runoff pathways, delaying runoff initiation. Additionally, the stabilized soil structure significantly enhanced erosion resistance, reducing net flow and sediment yield (Roshan et al., 2020; Vakili et al., 2022). However, due to the limited adsorption capacity of soil colloids, increasing the L concentration created alternating zones of localized oversaturated cementation and non-cemented regions. Unreacted L also promoted particle slippage under compression. Ice crystals preferentially grew in weakly cemented zones, propagating cracks along cementation boundaries and forming wider, more extensive fracture networks. Although L2 soils exhibited denser structures, their brittleness increased, resulting in wider cracks and heightened runoff resistance. Consequently, runoff initiation for L2 occurred later than L1, with lower runoff volume. The high-concentration cementation in L2 enhanced macroscale structural stability but concentrated runoff energy within widened cracks, accelerating flow velocity and scouring capacity. This process generated localized erosion hotspots (Khajeh et al., 2024), which mobilized more soil particles, expanded erosion areas, and intensified runoff erosivity. As a result, L2 produced substantially higher sediment yields than L1, with post-erosion surfaces exhibiting greater roughness.

P significantly optimizes soil hydrological processes and erosion resistance through its unique dual mechanism of water absorption and cementation. It enhances pore connectivity and expands pore sizes, improving saturated hydraulic conductivity and promoting the infiltration of supersaturated surface moisture, thereby effectively delaying runoff initiation (Chen et al., 2016). In this study, P1 delayed runoff initiation by 50.3 % compared to the CK. However, Ajwa and Trout (2006) reported that P increases solution viscosity, which may reduce infiltration when applied via irrigation water. This discrepancy may arise from three factors: (1) Molecular weight variation: Higher molecular weight P increases solution viscosity, hindering free water movement and reducing infiltration (Chen et al., 2016); (2) Soil texture specificity: P enhances infiltration in fine- and medium-textured soils but exhibits weaker effects in coarse-textured soils (He et al., 2007; Sojka et al., 1998); (3) Application method: Infiltration is primarily governed by pore morphology and connectivity (Albalasmeh et al., 2021). In this study, P was thoroughly mixed with soil to maximize pore expansion and connectivity, contrasting with surface application in irrigation-based studies.

Furthermore, the hydrogel film formed by P exhibits elasticity, effectively reducing the kinetic energy of raindrop impact and mitigating soil erosion risks. Additionally, by leveraging the high cation exchange capacity (CEC) of black soil, P enhances cation bridging processes. The long polymer chains of P facilitate binding to multiple soil particle surfaces, increasing aggregate stability, strengthening erosion resistance, and reducing sediment yield in runoff (Chen et al., 2016; Green et al., 2000). Although raindrops create slight impact craters on the soil surface, gradually increasing surface roughness, higher P concentrations reduce soil permeability, shortening runoff initiation time and increasing total runoff volume. This further enhances soil erosion resistance. Consequently, P2 demonstrates significant advantages in improving soil erosion resistance and reducing soil and water loss (Albalasmeh et al., 2021; Sadeghi et al., 2020).

5. Conclusion

This study utilized a self-designed wind tunnel-rainfall test setup to investigate the effects of different soil amendments on the soil hydrothermal environment, structural stability, and erosion characteristics under compound erosion conditions. The results demonstrated that 1.0 % concentration treatments (L1 and P1) significantly enhanced ST, LVWC upper limit, and MWD. Specifically, L1 increased these parameters by 28.0 %, 29.6 %, and 233.1 %, respectively, while P1 enhanced them by 57.5 %, 43.6 %, and 554.0 %, respectively, compared to the CK. Increasing the concentration to 2.0 % (L2) further improved thermal insulation and water retention capacity, reducing temperature fluctuations by 8.7 % and increasing LVWC upper limit by 14.4 %. The enhanced soil properties resulted in improved erosion resistance, as evidenced by L2 and P2 reducing total runoff and sediment yield by 82.0 %–80.4 % and 30.3 %–99.2 %, respectively. However, H exhibited limited effectiveness, with higher concentrations ($\geq$2.0 %) significantly decreasing water holding capacity and aggregate stability, consequently increasing runoff and sediment yield. Principal component analysis identified P2 as the most effective amendment for comprehensive soil improvement.

While this study elucidates the mechanisms of amendments on soil physical properties and erosion characteristics, it does not establish a complete concentration-response relationship. The observed reduction in available water content at higher concentrations highlights the need for further research to optimize amendment concentrations for agricultural applications. These findings provide strategic solutions for controlling compound erosion and conserving soil resources in Northeast China's black soil region.

CRediT authorship contribution statement

Xu Leng: Writing – original draft, Methodology, Data curation, Investigation, Formal analysis, Conceptualization. **Heng Li:** Writing – original draft, Investigation, Conceptualization. **Qiang Fu:** Writing – review & editing, Conceptualization, Funding acquisition, Investigation, Methodology, Resources. **Tianxiao Li:** Writing – review & editing, Funding acquisition, Resources, Software. **Renjie Hou:** Formal analysis, Funding acquisition, Project administration, Resources. **Mo Li:** Writing – review & editing. **Dong Liu:** Writing – review & editing. **Zhaoqiang Zhou:** Writing – review & editing. **Di Wu:** Writing–review & editing.

Declaration of Competing interest

The authors declare that they have no known competing financial interests or personal relationships that could have appeared to influence the work reported in this paper.

Acknowledgment

This research has been supported by funds from the National Natural Science Foundation of China (52179033); The Joint Fund of the National Natural Science Foundation of China (U20A20318); The National Science Fund for Distinguished Young Scholars (51825901); The National Natural Science Foundation of China (52279035); The Heilongjiang Provincial Science Fund for Distinguished Young Scholars (YQ2022E007).

Data availability

Data will be made available on request.

References

Abu-Hamdeh, N.H., 2003. Thermal properties of soils as affected by density and water content. Biosyst. Eng. 86 (1), 97–102.
Adjuik, T.A., Nokes, S.E., Montross, M.D., Wendroth, O., 2022. The impacts of Bio-Based and synthetic hydrogels on soil hydraulic properties: a review. Polymers 14 (21), 4721.
Ajwa, H.A., Trout, T.J., 2006. Polyacrylamide and water quality effects on infiltration in sandy loam soils. Soil Sci. Soc. Am. J. 70 (2), 643–650.
Albalasmeh, A.A., Hamdan, E.H., Gharaibeh, M.A., El Hanandeh, A., 2021. Improving aggregate stability and hydraulic properties of sandy loam soil by applying polyacrylamide polymer. Soil Tillage Res. 206, 104821.
An, M., Han, Y., Zhao, C., Qu, Z., Xu, P., Wang, X., He, X., 2022. Effects of different wind directions on soil erosion and nitrogen loss processes under simulated wind-driven rain. Catena 217, 106423.
Andry, H., Yamamoto, T., Irie, T., Moritani, S., Inoue, M., Fujiyama, H., 2009. Water retention, hydraulic conductivity of hydrophilic polymers in sandy soil as affected by temperature and water quality. J. Hydrol. 373 (1-2), 177–183.
Ariyanta, H.A., Sari, F.P., Sohail, A., Restu, W.K., Septiyanti, M., Aryana, N., Fatriasari, W., Kumar, A., 2023. Current roles of lignin for the agroindustry: applications, challenges, and opportunities. Int. J. Biol. Macromol. 240, 124523.
Borrelli, P., Alewell, C., Yang, J.E., Bezak, N., Chen, Y., Fenta, A.A., Fendrich, A.N., Gupta, S., Matthews, F., Modugno, S., Haregeweyn, N., Robinson, D.A., Tan, F., Vanmaercke, M., Verstraeten, G., Vieira, D.C.S., Panagos, P., 2023. Towards a better understanding of pathways of multiple co-occurring erosion processes on global cropland. Int. Soil Water Conserv. Res. 11 (4), 713–725.
Chen, Q., Indraratna, B., 2015. Shear behaviour of sandy silt treated with lignosulfonate. Can. Geotech. J. 52 (8), 1180–1185.
Chen, Z., Chen, W., Li, C., Pu, Y., Sun, H., 2016. Effects of polyacrylamide on soil erosion and nutrient losses from substrate material in steep rocky slope stabilization projects. Sci. Total Environ. 554 26–33.
Cordeiro, F.C., Santa-Catarina, C., Silveira, V., de, Souza, S.R., 2011. Humic acid effect on catalase activity and the generation of reactive oxygen species in corn (Zea mays). Biosci. Biotechnol. Biochem. 75 (1), 70–74.
Dong, C., Huang, Y., Zhang, W., Tang, X., Gu, Y., Feng, Y., 2023. Behavioral evaluation on the engineering properties of lignin-stabilized loess: reuse of renewable materials. Constr. Build. Mater. 369, 130599.
Fangueiro, D., Kidd, P.S., Alvarenga, P., Beesley, L., Varennes, A.D., 2018. Strategies for soil protection and remediation. Soil Pollut. 251–281.
Fernandez-Raga, M., Palencia, C., Keesstra, S., Jordan, A., Fraile, R., Angulo-Martinez, M., Cerda, A., 2017. Splash erosion: a review with unanswered questions. EarthSci. Rev. 171, 463–477.
Ferrick, M.G., Gatto, L.W., 2005. Quantifying the effect of a freeze-thaw cycle on soil erosion: laboratory experiments. Earth Surf. Process. Landf. 30 (10), 1305–1326.
Green, V.S., Stott, D.E., Norton, L.D., Graveel, J.G., 2000. Polyacrylamide molecular weight and charge effects on infiltration under simulated rainfall. Soil Sci. Soc. Am. J. 64 (5), 1786–1791.
Gumus, I., Seker, C., 2015. Influence of humic acid applications on modulus of rupture, aggregate stability, electrical conductivity, carbon and nitrogen content of a crusting problem soil. Solid Earth 6 (4), 1231–1236.
He, J., Cai, Q., Tang, Z., 2007. Wind tunnel experimental study on soil wind erosion control with PAM. J. Soil Water Conserv. 21 (2), 12–15.
He, Y., Gu, F., Xu, C., Wang, Y., 2019. Assessing of the influence of organic and inorganic amendments on the physical-chemical properties of a red soil (Ultisol) quality. Catena 183, 104231.
Ji, Y., Wang, H., Li, X., Zhao, P., Wang, Q., Li, R., Vandeginste, V., 2023. Effect of anionic polyacrylamide polymer on frost heave mitigation and its implication for Frost-Susceptible soil. Polymers 15 (9), 2096.
Jiang, T., Teng, L., Wei, S., Deng, L., Luo, Z., Chen, Y., Flanagan, D.C., 2010. Application of polyacrylamide to reduce phosphorus losses from a Chinese purple soil: a laboratory and field investigation. J. Environ. Manag. 91 (7), 1437–1445.
Jiang, Y., Zheng, F., Wen, L., Shen, H., 2019. Effects of sheet and rill erosion on soil aggregates and organic carbon losses for a mollisol hillslope under rainfall simulation. J. Soils Sediment. 19 (1), 467–477.
Jiang, Z., Yang, H., Ji, Z., Pan, Q., Ye, Z., Yu, X., Su, G., Zheng, Y., 2024. Lignocellulosic hydrogel for profile control and water plugging in high salt reservoirs. J. Mol. Liq. 401, 124707.

Khajeh, A., Nazari, Z., Movahedrad, M., Vakili, A.H., 2024. A state-of-the-art review on the application of lignosulfonate as a Green alternative in soil stabilization. Sci. Total Environ. 943, 173500.
Kinnell, P.I.A., 2022. Insights into the sediment transport processes operating in rain-impacted flows. Catena 217, 106452.
Koohpeyma, H.R., Vakili, A.H., Moayedi, H., Panjsetooni, A., Nazir, R., 2013. Investigating the effect of lignosulfonate on erosion rate of the embankments constructed with clayey sand. Sci. World J., 587462
Lal, R., 2019. Accelerated soil erosion as a source of atmospheric CO_2. Soil Tillage Res. 188, 35–40.
Leuther, F., Schlueter, S., 2021. Impact of freeze-thaw cycles on soil structure and soil hydraulic properties. Soil 7 (1), 179–191.
Li, P., Xu, G., Lu, K., Zhang, X., Shi, P., Bai, L., Ren, Z., Pang, G., Xiao, L., Gao, H., Pan, M., 2019. Runoff change and sediment source during rainstorms in an ecologically constructed watershed on the loess plateau, China. Sci. Total Environ. 664, 968–974.
Li, X., Li, P., Chen, W., Ren, J., Wu, W., 2023. Preparation and adsorption properties of Lignin/Cellulose hydrogel. Materials 16 (12), 4260.
Liang, Y., Yeh, T.C.J., Ma, C., Zhang, J., Xu, W., Yang, D., Hao, Y., 2021. Experimental investigation on hole erosion behaviors of chemical stabilizer treated soil. J. Hydrol. 594, 125647.
Liu, H., Hu, Y., Hao, Y., Yan, X., Wu, L., Wang, C., Li, X., 2022. Progressive freeze-thaw redistributes water, solute and CO_2 emissions across soil layers - the role of soil particle size. Catena 219, 106614.
Liu, Q., Zhang, Z., Zhang, S., Li, X., Long, H., Meng, X., Melnikov, A., Gagarin, L., 2023. The influence of particle morphology on the long-term strength of sandy soil under freeze-thaw cycles. Case Stud. Constr. Mater. 18, E02196.
Liu, T., Xu, X., Yang, J., 2017. Experimental study on the effect of freezing-thawing cycles on wind erosion of black soil in northeast China. Cold Reg. Sci. Technol. 136, 1–8.
Liu, X., Zheng, D., Pan, Z., Lin, Q., Tuo, D., 2006. Effects of inoculated rhizobia and humic-acid fertilizer in soil on wind erosion. J. Soil Water Conserv. 20 (1), 68–71, 90.
Liu, Y., Chang, M., Wang, Q., Wang, Y., Liu, J., Cao, C., Zheng, W., Bao, Y., Rocchi, I., 2020. Use of Sulfur-Free lignin as a novel soil additive: a multi-scale experimental investigation. Eng. Geol. 269, 105551.
Lu, S., Ren, T., Gong, Y., Horton, R., 2007. An improved model for predicting soil thermal conductivity from water content at room temperature. Soil Sci. Soc. Am. J. 71 (1), 8–14.
Lu, Y., Lu, S., Horton, R., Ren, T., 2014. An empirical model for estimating soil thermal conductivity from texture, water content, and bulk density. Soil Sci. Soc. Am. J. 78 (6), 1859–1868.
Marzen, M., Iserloh, T., Casper, M.C., Ries, J.B., 2015. Quantification of particle detachment by rain splash and wind-driven rain splash. Catena 127, 135–141.
Mhaske, S.N., Pathak, K., Basak, A., 2019. A comprehensive design of rainfall simulator for the assessment of soil erosion in the laboratory. Catena 172, 408–420.
Mulualem, T., Adgo, E., Meshesha, D.T., Tsunekawa, A., Haregeweyn, N., Tsubo, M., Kebede, B., Mamedov, A.I., Masunaga, T., Berihun, M.L., 2021. Examining the impact of polyacrylamide and other soil amendments on soil fertility and crop yield in contrasting agroecological environments. J. Soil Sci. Plant Nutr. 21 (3), 1817–1830.
Park, H.J., Chae, N., Sul, W.J., Lee, B.Y., Lee, Y.K., Kim, D., 2015. Temporal changes in soil bacterial diversity and humic substances degradation in subarctic tundra soil. Microb. Ecol. 69 (3), 668–675.
Rodrigues Sousa, H., Lima, I.S., Neris, L.M.L., Silva, A.S., Santos Nascimento, A.M.S., Araujo, F.P., Ratke, R.F., Silva, D.A., Osajima, J.A., Bezerra, L.R., Silva-Filho, E.C., 2021. Superabsorbent hydrogels based to Polyacrylamide/Cashew tree gum for the controlled release of water and plant nutrients. Molecules 26 (9), 2680.
Roshan, K., Choobbasti, A.J., Kutanaei, S.S., 2020. Evaluation of the impact of fiber reinforcement on the durability of lignosulfonate stabilized clayey sand under wet-dry condition. Transp. Geotech. 23, 100359.
Sadeghi, S.H., Kiani-Harchegani, M., Hazbavi, Z., Sadeghi, P., Angulo-Jaramillo, R., Lassabatere, L., Younesi, H., 2020. Field measurement of effects of individual and combined application of biochar and polyacrylamide on erosion variables in loess and marl soils. Sci. Total Environ. 728, 138866.
Sarker, T.C., Zotti, M., Fang, Y., Giannino, F., Mazzoleni, S., Bonanomi, G., Cai, Y., Chang, S.X., 2022. Soil aggregation in relation to organic amendment: a synthesis. J. Soil Sci. Plant Nutr. 22 (2), 2481–2502.
Sela, S., Svoray, T., Assouline, S., 2014. Soil surface sealing effect on soil moisture at a semiarid hillslope: implications for remote sensing estimation. Remote Sens. 6 (8), 7469–7490.
Semenov, V.M., Tulina, A.S., Semenova, N.A., Ivannikova, L.A., 2013. Humification and nonhumification pathways of the organic matter stabilization in soil: a review. Eurasia Soil Sci. 46 (4), 355–368.
Shao, F., Zeng, S., Wang, Q., Tao, W., Wu, J., Su, L., Yan, H., Zhang, Y., Lin, S., 2023. Synergistic effects of biochar and carboxymethyl cellulose sodium (CMC) applications on improving water retention and aggregate stability in desert soils. J. Environ. Manag. 331, 117305.
Sojka, R., Lentz, E., R., D, 1998. Water and erosion management with multiple applications of polyacrylamide in furrow irrigation. Soil Sci. Soc. Am. J. 62 (6), 1672-1672.
Starkloff, T., Larsbo, M., Stolte, J., Hessel, R., Ritsema, C., 2017. Quantifying the impact of a succession of freezing-thawing cycles on the pore network of a silty clay loam and a loamy sand topsoil using X-ray tomography. Catena 156, 365–374.
Sun, B., Liu, J., Ren, F., Li, H., Zhang, G., Ma, J., Ma, B., Li, Z., 2022. Effects of seasonal freeze-thaw and wind erosion on runoff and sediment yields of three loamy slopes of loess plateau, China. Catena 215, 106309.
Szczerski, C., Naguit, C., Markham, J., Goh, T.B., Renault, S., 2013. Short- and Long-Term effects of modified humic substances on soil evolution and plant growth in gold mine tailings. Water Air Soil Pollut. 224 (3), 1–14.
Tajdini, M., Bonab, M.H., Golmohamadi, S., 2018. An experimental investigation on effect of adding natural and synthetic fibres on mechanical and behavioural parameters of soil-cement materials. Int. J. Civ. Eng. 16 (4B), 353–370.
Ta'negonbadi, B., Noorzad, R., 2017. Stabilization of clayey soil using lignosulfonate. Transp. Geotech. 12, 45–55.
Thomsen, L.M., Baartman, J.E.M., Barneveld, R.J., Starkloff, T., Stolte, J., 2015. Soil surface roughness: comparing old and new measuring methods and application in a soil erosion model. Soil 1 (1), 399–410.
Turan, M.A., Asik, B.B., Katkat, A.V., Celik, H., 2011. The effects of Soil-Applied humic substances to the dry weight and mineral nutrient uptake of maize plants under Soil-Salinity conditions. Not. Bot. Horti Agrobot. Cluj. Napoca 39 (1), 171–177.
Vakili, A.H., Ghasemi, J., bin Selamat, M.R., Salimi, M., Farhadi, M.S., 2018. Internal erosional behaviour of dispersive clay stabilized with lignosulfonate and reinforced with polypropylene fiber. Constr. Build. Mater. 193, 405–415.
Vakili, A.H., Salimi, M., Lu, Y., Shamsi, M., Nazari, Z., 2022. Strength and post-freeze-thaw behavior of a marl soil modified by lignosulfonate and polypropylene fiber: an environmentally friendly approach. Constr. Build. Mater. 332, 127364.
Van Pelt, R.S., Hushmurodov, S.X., Baumhardt, R.L., Chappell, A., Nearing, M.A., Polyakov, V.O., Strack, J.E., 2017. The reduction of partitioned wind and water erosion by conservation agriculture. Catena 148, 160–167.
Vinod, J.S., Indraratna, B., Mahamud, M.A.A., 2010. Stabilisation of an erodible soil using a chemical admixture. Proc. Inst. Civ. Eng. Ground Improv. 163 (1), 43–51.
Wang, L., Zuo, X., Zheng, F., Wilson, G.V., Zhang, X.J., Wang, Y., Fu, H., 2020. The effects of freeze-thaw cycles at different initial soil water contents on soil erodibility in Chinese mollisol region. Catena 193, 104615.
Wang, M., Zhu, Y., Zhao, T., Cui, L., Mao, W., Ye, M., Wu, J., Yang, J., 2022. Chemical characteristics of salt migration in frozen soils during the freezing-thawing period. J. Hydrol. 606, 127403.
Wang, W., Yin, S., Yu, J., He, Z., Xie, Y., 2023. Long-term trends of precipitation and erosivity over northeast China during 1961-2020. Int. Soil Water Conserv. Res. 11 (4), 743–754.
Wang, Y., Zheng, F., Zhou, X., Qin, C., Fu, H., Zuo, X., Liu, G., Zhang, J., 2019. Soil profile temperature variation in farmlands during Freeze-thaw period in mollisol region. Bull. Soil Water Conserv. 39 (3), 57–64.
Wei, X., Yuan, X., Li, Y., Wang, Y., Yuan, X., 2011. Research on the Water-saving and Yield-increasing effect of polyacrylamide. Procedia Environ. Sci. 11, 573–580.
Wu, T., Li, H., Lyu, H., 2023. Effect of freeze-thaw process on heat transfer and water migration between soil water and groundwater. J. Hydrol. 617, 128987.
Xu, S., Zhang, L., McLaughlin, N.B., Mi, J., Chen, Q., Liu, J., 2015. Effect of synthetic and natural water absorbing soil amendment soil physical properties under potato production in a semi-arid region. Soil Tillage Res. 148, 31–39.
Xue, P., Fu, Q., Li, T., Liu, D., Hou, R., Li, Q., Li, M., Meng, F., 2022. Effects of biochar and straw application on the soil structure and water-holding and gas transport capacities in seasonally frozen soil areas. J. Environ. Manag. 301, 113943.
Yang, J., Li, S., Di, H., Liu, D., Wang, X., Zhao, Y., 2024. Influence of anionic polyacrylamide on the freeze-thaw resistance of silty clay. Cold Reg. Sci. Technol. 219, 104111.
Zhang, F., Wang, M., Yang, M., 2021. Successful application of the taguchi method to simulated soil erosion experiments at the slope scale under various conditions. Catena 196, 104835.
Zhang, X.J., 2023. Roles of raindrop impact in detachment and transport processes of interrill soil erosion. Int. Soil Water Conserv. Res. 11 (4), 592–601.
Zhang, Z., Luo, J., Chen, B., 2020. Spatially explicit quantification of total soil erosion by RTK GPS in wind and water eroded croplands. Sci. Total Environ. 702, 134716.
Zhao, Y., Hu, X., 2023. A pore-scale investigation of soil aggregate structure responding to freeze-thaw cycles using X-ray computed microtomography. J. Soils Sediment. 23 (8), 3137–3148.
Zhu, X., Liu, W., Yuan, X., Chen, C., Zhu, K., Zhang, W., Yang, B., 2022. Aggregate stability and size distribution regulate rainsplash erosion: evidence from a humid tropical soil under different land-use regimes. Geoderma 420, 115880.
Zuo, Y., Meng, F., Li, T., Fu, Q., Liu, D., Hou, R., Li, Q., Li, M., 2022. Effect of biochar application on freezing-thawing deformation of farmland soil during freeze-thaw cycling. Geoderma 405, 115510.